Room Temperature Synthesis Mediated Porphyrinic NanoMOF Enables Benchmark Electrochemical Biosensing

Zhenyu Zhou, Jun Wang,* Shujin Hou, Soumya Mukherjee,* and Roland A. Fischer*

Leveraging size effects, nanoparticles of metal-organic frameworks, nano-MOFs, have recently gained traction, amplifying their scopes in electrochemical sensing. However, their synthesis, especially under eco-friendly ambient conditions remains an unmet challenge. Herein, an ambient and fast secondary building unit (SBU)-assisted synthesis (SAS) route to afford a prototypal porphyrinic MOF, Fe-MOF-525 is introduced. Albeit the benign room temperature conditions, Fe-MOF-525(SAS) nanocrystallites obtained are of ≈30 nm size, relatively smaller than the ones conventional solvothermal methods elicit. Integrating Fe-MOF-525(SAS) as a thin film on a conductive indium tin oxide (ITO) surface affords Fe-MOF-525(SAS)/ITO, an electrochemical biosensor. Synergistic confluence of modular MOF composition, analyte-specific redox metalloporphyrin sites, and crystal downsizing contribute to its benchmark voltammetric uric acid (UA) sensing. Showcasing a wide linear range of UA detection with high sensitivity and low detection limit, this SAS strategy coalesces ambient condition synthesis and nanoparticle size control, paving a green way to advanced sensors.

Z. Zhou, J. Wang
School of Chemistry and Chemical Engineering
Nanchang University
Nanchang 330031, P. R. China
E-mail: jwang7@ncu.edu.cn

S. Hou
Physics of Energy Conversion and Storage
Physic-Department
Technische Universität München
James-Franck-Str. 1, 85748 Garching, Germany

S. Mukherjee
Department of Chemical Sciences
Bernal Institute
University of Limerick
Limerick V94T9PX, Ireland
E-mail: soumya.mukherjee@ul.ie

S. Mukherjee, R. A. Fischer
Chair of Inorganic and Metal-Organic Chemistry
Department of Chemistry
Technische Universität München
Lichtenbergstraße 4, 85748 Garching b. München, Germany
E-mail: roland.fischer@tum.de

ⓘD The ORCID identification number(s) for the author(s) of this article can be found under https://doi.org/10.1002/smll.202301933.

1. Introduction

Metal–organic frameworks (MOFs) are an emerging class of by-design porous materials, primarily, crystalline solids afforded from the bottom-up self-assembly of organic linkers and inorganic metal clusters.[1] The latter is also known as secondary building units (SBUs).[2] Relying upon the first principles of crystal engineering,[3] MOFs feature an amenability to porosity control by tapping their compositional modularity.[4] Thanks to their guest-accessible surface areas, and a tailored control over pore sizes and/or pore environments, MOFs have demonstrated benchmark properties in sensing,[5] catalysis,[6] gas storage,[7] and separation.[8] Specifically for electrochemical sensing, porphyrinic MOFs (PP-MOFs) largely benefit from porphyrin struts functioning as active sites.[5b,9] Reaping benefits from the π-conjugated macrocyclic scaffolds, porphyrins and metalloporphyrins present high electron transfer and selective redox catalysis, eliciting electrocatalytic sensing in PP-MOFs.[5b,10] Albeit several recent examples in this regard, influences of particle size remain ignored.[9,11] As an intrinsic feature of MOF crystals, particle size is primed to culminate in size-dependent electrochemical sensing.[12] With decreasing particle size, MOFs can exhibit significantly enhanced physical and chemical properties compared to their bulk counterparts, such as increased external surface areas. This results in an increased exposure to the external active sites.[13] Unsurprisingly, controlled downsizing of MOF crystals across the nanoscale regime should catalyze the likelihood to further harness their pore structures and/or surface reactivities. Conversely, thus far, preparing a number of MOFs, including PP-MOFs, heavily rely upon conventional solvothermal synthesis (CSS). These typically involve high temperature treatment for several days to weeks,[5b,12b,14] entailing a massive energy footprint. With improved sustainability at focus, time and energy pose major handicaps in transitioning MOFs into commercial adoption.[15] To address this, a simple and rapid room temperature (RT) synthesis of MOFs is a desired advance from techno-economic and eco-friendly perspectives.[16]

Despite the unique benefits of RT synthesis and particle size effects, their dual realization remains a challenge. Thus far, only a handful of methods, viz., mechanical grinding, microwave-assisted method, electric field-controlled synthesis, microfluidic synthesis, surfactant-assisted growth,

**ADVANCED
SCIENCE NEWS**
www.advancedsciencenews.com

NANO · MICRO
small
www.small-journal.com

and coordination modulation are known to afford MOF nanoparticles.[13a,17] However, these either require a special set-up, or the downsizing of MOF crystallites to <50 nm is cumbersome. Simply put, facile and energy-/or cost-efficient synthesis of small MOF nanoparticles remains an unmet challenge. In addition, understanding the effects of particle size modulation on MOF properties is still in its infancy, and warrants critical interrogation.[13b,17d] For RT synthesis, only a few examples hitherto exist. These are limited to MOFs with relatively low connected (≤6) nodes, MOF-5, ZIF-8 and HKUST-1, inter alia.[18] High-connected (≥8) MOFs featuring complicated topologies typically require high activation energy (e.g., solvothermal, and/or hydrothermal conditions).[14a,19] Besides, high-connected MOFs, such as the Zr(IV)-based PP-MOFs are well-known to demonstrate high thermal/chemical/hydrolytic stability and pore environments amenable to crystal engineering principles.[5b,14a,20] Collectively, these aspects culminate in a range of sensing applications, and an effective RT synthesis will enable easier transition to higher technological readiness levels.

Herein, an SBU-assisted synthesis (SAS) strategy was developed to enable the RT formation of high-connected MOF crystals, homogeneously downsized to <50 nm. A prototypical MOF self-assembly comprises a) the initial nucleation and formation of SBUs, and b) linker assembly to elicit an extended reticular structure.[2] In this context, the SAS approach harnessing SBUs as reactants features unique merits. Sustained by well-defined organic linkers, a preformed SBU with determinate geometry and connectivity forms can eliminate the serendipity in coordination, contributing to the formation of target MOFs.[2b,21]

Conversely, compared to direct MOF formation from metal ions/clusters and organic linkers, using preformed SBUs as reactants is primed to reduce the activation energy barrier, expediting the reaction kinetics. This, in effect, enables rapid room-temperature synthesis of MOFs, lowering the energy footprint substantially.[22] To this end, SBU-assisted rapid MOF assembly also tends to yield smaller nanocrystals, downsizing them further below 50 nm. Despite few successful examples of SAS,[23] a RT method to prepare small-size high-connected MOF nanocrystals remains unknown, as we introduce it herein.

Exemplifying a PP-MOF, we prepare $[Zr_6O_4(OH)_4(Fe-TCPP)_3]$, Fe-MOF-525 nanocrystals via the SAS approach at RT (**Figure 1**b).[14a] Specifically, Fe-MOF-525 is constructed from 12-connected Zr_6 clusters and 4-connected iron tetrakis(4-carboxyphenyl)-porphyrin (Fe-TCPP) ligands (Figure 1a). Of particular importance is its high surface area, >2000 m^2 g^{-1} and 1D quadrangular micropore ≈1.6 nm (Figure S1, Supporting Information).[14a,19d] Meanwhile, the reticular pores of Fe-MOF-525 replete with redox-active porphyrin sites contribute to an increased propensity for the analytes to get concentrated and selectively identified. This endows Fe-MOF-525 with a high predisposition to enable electrocatalytic sensing.[5b,24] In this study, a sensor is fabricated by uniformly coating Fe-MOF-525(SAS) film on conductive indium tin oxide (ITO) glass as Fe-MOF-525(SAS)/ITO electrode (Figure 1b). Monitoring its electrochemical sensing properties, furthermore, a detailed investigation into particle size effects is conducted.

2. Results and Discussion

Zr(IV)-based PP-MOFs are typically synthesized using hazardous, high-boiling solvents (e.g., *N,N*-Dimethylformamide, *N,N*-diethylformamide) and high temperature/pressure, while their room-temperature synthesis is relatively difficult due to the sluggish kinetics of nucleation and crystallization.[12b,14a,20b,d] Nevertheless, preformed SBUs not only function as a primer for efficient coordination, but also lower the activation energy barrier to accelerate reaction kinetics of the framework assembly. This, in turn, enables the rapid RT synthesis of Zr-based PP-MOFs.[2b,22a] Herein, in pursuit of the RT synthesis of Fe-MOF-525 nanocrystals via SAS method, Zr_6 cluster SBUs are the prerequisites and are successfully prepared (Figure S2, Supporting Information).[25] Benefiting from the preformed SBUs, the Fe-MOF-525 was synthesized following a typical recipe (Table S1, Supporting Information), named Fe-MOF-525(SAS), hereinafter. Powder X-ray diffraction (PXRD) pattern of Fe-MOF-525(SAS) exhibits consistency with the simulated one, indicating its phase purity (Figure 1c).[14a] Porosity of Fe-MOF-525(SAS) is examined by a cryogenic N_2 adsorption experiment. A typical type-I isotherm suggests microporosity with a pore size of ≈1.6 nm (Figure 1d). Applying Rouquerol criteria to the 77 K N_2 isotherm, the Brunauer–Emmett–Teller surface area is determined as high as 2193 m^2 g^{-1}.[26] Large 1D channels and high surface area, in principle, should prove beneficial to enable rapid analyte aggregation and mass transport for efficient sensing.[5b] Attenuated total reflection infrared (ATR-IR) spectra are recorded to identify the compositions of the prepared Fe-MOF-525(SAS) (Figure 1e). Compared to the free H_2TCPP, the metallisation of Fe-TCPP ligand is evidenced by disappearance of the N–H characteristic peak at 960 cm^{-1} and appearance of a new peak at 998 cm^{-1} assigned to Fe-N bonds.[11b,27] The latter signature is also found in the Fe-MOF-525(SAS). This aligns well with the energy-dispersive X-ray spectroscopy and ultraviolet-visible spectroscopy (UV–vis) spectra (Figures S3 and S4, Supporting Information). Moreover, in contrast to the spectrum of Fe-TCPP, Fe-MOF-525(SAS) exhibits an absence of stretching vibration around 1695 cm^{-1} (C=O bonds) whereas a strong peak at 1424 cm^{-1} (COO symmetric stretch band) appears, reflecting the coordination of carboxyl groups in Fe-TCPP with Zr_6 clusters for the formation of Fe-MOF-525(SAS) nanocrystals.[5b,19d] ^1H nuclear magnetic resonance spectroscopy, ^1H NMR data recorded on the digested Fe-MOF-525(SAS) reveals the absence of any methacrylate ligand, indicating the defect-free nature of Fe-MOF-525(SAS) (Figure S5, Supporting Information). Scanning electron microscopy (SEM) shows the Fe-MOF-525(SAS) nanoparticles with the size of 30.50 ± 3.05 nm, much smaller than the previous reports which vary from hundreds to thousands of nanometres (Figure 1f).[12b,14c,24a] The Tyndall effect observed in the colloidal suspension of Fe-MOF-525(SAS) is also consistent with the nanocrystallites' dimensions (Figure S6, Supporting Information).[17e] In principle, such uniform Fe-MOF-525(SAS) nanoMOF should indeed lead to an efficient electrochemical sensor, when coated upon a conductive ITO surface.[12b]

To further understand the SAS mediated formation of Fe-MOF-525(SAS) nanoMOF, the classical LaMer model is applied to analyze the procedure (Figure 1g). The LaMer mode is
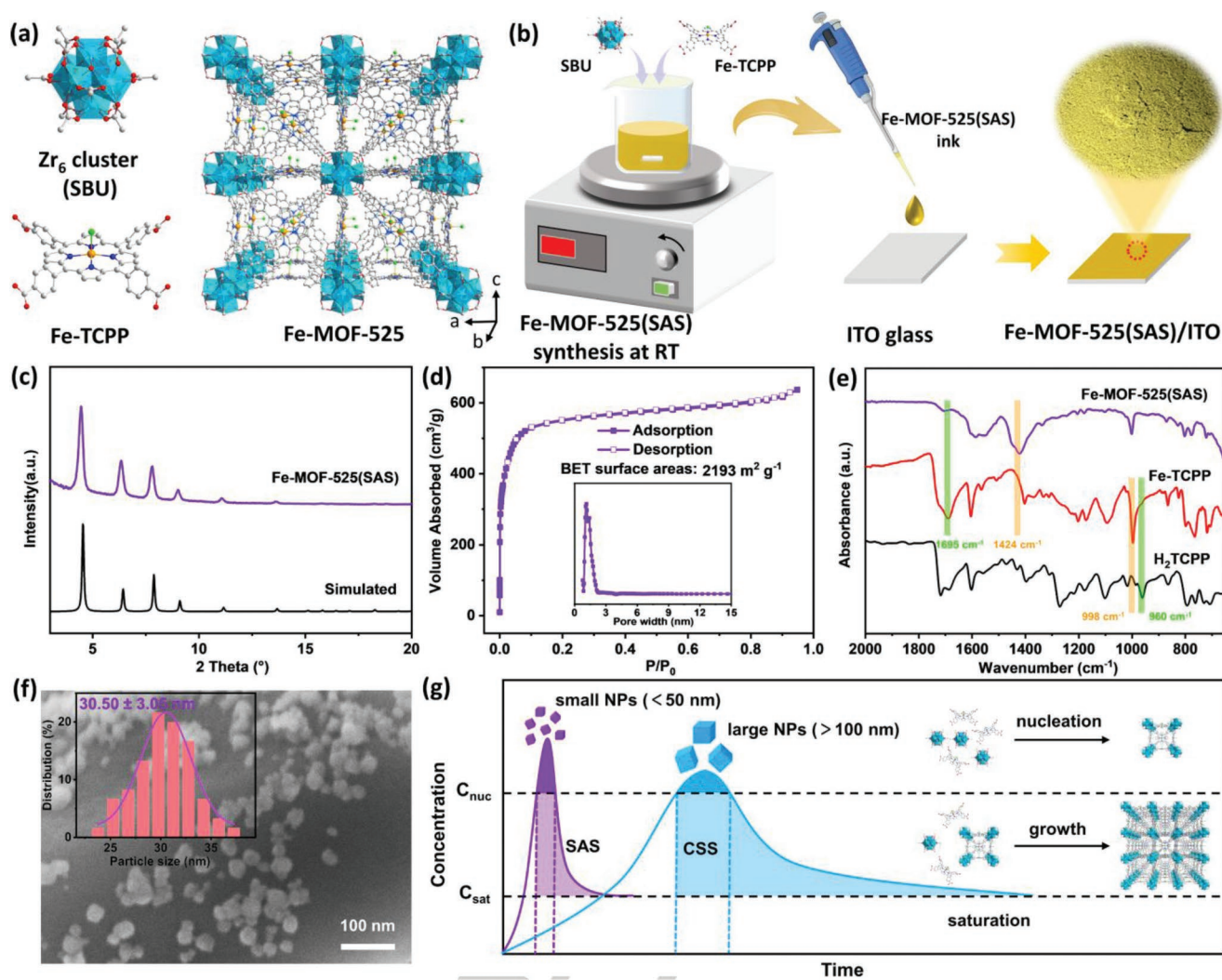
ADVANCED
SCIENCE NEWS
www.advancedsciencenews.com

NANO · MICRO
small
www.small-journal.com

Figure 1. a) Structures of the building blocks: Zr$_6$ cluster (SBU) and Fe-TCPP ligand sustaining Fe-MOF-525; the framework structure of Fe-MOF-525. H atoms are omitted for clarity. Color scheme: C, gray; O, red; N, blue; Cl, olive green and Fe, yellow. b) Schematic illustration of the SAS for Fe-MOF-525 preparation and coating route leading to a Fe-MOF-525(SAS)/ITO electrode. c) Simulated and experimental PXRD patterns of the bulk Fe-MOF-525(SAS) synthesized at a typical synthetic recipe: 0.6 mm SBU, r_{SBU} 800 eq., RT, 3 h. d) N$_2$ sorption isotherms for Fe-MOF-525(SAS) at 77 K (solid and open symbols denote adsorption and desorption, respectively). Inset shows density functional theory based pore size distribution profile for Fe-MOF-525(SAS) from the N$_2$ isotherm recorded at 77 K. e) ATR-IR spectra for the free ligands H$_2$TCPP, Fe-TCPP, stacked alongside that for Fe-MOF-525(SAS). f) SEM image of Fe-MOF-525(SAS). Inset: particle size distribution plot of Fe-MOF-525(SAS) nanocrystals. g) Schematic illustration of the LaMer Model accounting for the MOF nanoparticle nucleation and growth. Purple trace: the synthesis of uniform small MOF nanoparticles benefiting from the preformed SBUs acting as abundant nuclei for rapid crystal nucleation and growth during SAS. Blue trace: confluence of a smaller number of nucleation sites and slow growth rate results in uniformly larger nanoparticles during CSS.

composed of two stages, i.e., nucleation and growth.[13a,13b,28] When the concentration of reactive species increases and exceeds the critical concentration of nucleation (C_{nuc}), the reactive species assemble to form nuclei, followed by further nucleation of the MOF unit cell. With decreasing reactant monomers, the nucleation ceases, followed by the growth until eventually reaching a particle growth and solvation equilibrium point (C_{sat}). According to the LaMer model, to obtain small and uniform MOF nanocrystals, it is essential to generate plentiful nuclei and coupled with a fast nucleation, then followed by the rapid termination of particle growth with depletion of reactive precursors.[13a,13b] Herein, in SAS process, a large number of preformed SBUs in system exactly serve as nuclei leading to

rapid nucleation and growth terminating in a short time, thus affording small Fe-MOF-525(SAS) nanoparticles, illustrated as the purple trace in Figure 1g. Conversely, CSS of MOF-525, without the assistance of preformed SBUs, the system undergoes a slow nucleation and the limited number of nucleation sites will slowly grow as large particles under the supply of abundant precursors (Figure 1g).[28] Following two commonly used solvothermal recipes,[12b,14a,c,24a,29] Fe-MOF-525(CSS1) and Fe-MOF-525(CSS2) were prepared. Consistent with the LaMer mode analysis, both variants register larger crystallite sizes of 145.37 ± 27.01 nm (Figures S7–S9, Supporting Information) and 764.10 ± 123.77 nm respectively (Figures S10–S12, Supporting Information).

ADVANCED
SCIENCE NEWS
www.advancedsciencenews.com

NANO · MICRO
small
www.small-journal.com

To critically interrogate particle size control in Fe-MOF-525(SAS) nanoMOF crystallites, the influences of several crucial parameters (i.e., modulator, concentration, reaction time, and temperature) were examined by altering the synthetic conditions (Table S1, Supporting Information). The modulators play essential roles in this SBU-assisted procedure of forming the nanocrystalline MOFs. This is because it not only contributes to the construction of crystalline MOFs, but also largely impact the morphologies of resulting MOFs, especially the particle size.[17f,19d,30] Thanks to containing the same coordinating group (i.e., carboxylate) as the porphyrin ligand, methacrylic acid as modulator delivers competitive SBU-ligand binding modes, thus slows down the reaction rate, allowing sophisticated incubation of MOF crystallites.[17f,19d,30] This is confirmed by the unsuccessful Fe-MOF-525(SAS) synthesis with sparsely added methacrylic acid additive at low modulator/SBUs ratios (r_{SBU}) of 100 and 200 equivalent (eq.) (Figures S13–S15, Supporting Information). With the stepwise increase of modulator amount (400–800 eq.), the synthesis of Fe-MOF-525(SAS) turned out with more success, accompanied by improved crystallinity and porosity (Figures S13, S14, S16, Supporting Information). An optimal modulator quantity of 800 eq. contributes to afford crystalline Fe-MOF-525(SAS) nanoparticles with small size (30.50 ± 3.05 nm). With the assurance of obtaining crystalline MOFs, low modulator concentrations were found to afford a fast MOF nucleation to generate plentiful MOF nuclei, then followed by the rapid termination of particle growth with depletion of reactive precursors. Indeed, such rapid growth yields small MOF crystals.[30] However, the addition of 1200 eq. of methacrylic acid largely restricts nucleation, resulting in fewer MOF nuclei for growth, ergo, larger crystals of size ≈71.60 ± 10.32 nm (Figure S16, Supporting Information).[30] Initial precursor concentrations are also found to impact the nucleation/crystallization, thus enabling a control over particle size. Low initial concentration is preferred to deliver nanoMOF particles, largely owing to the absence of adequate precursors for particle growth, post nucleation.[30] By changing the precursor concentrations (0.3–1.2 mM), the mean sizes of Fe-MOF-525(SAS) are regulated from 17.92 to 72.84 nm (Figures S17–S19, Supporting Information). However, despite a small particle size, the premature growth at such low concentration of 0.3 mM leads to poor MOF crystallinity and compromised porosity. Conversely, nanoMOFs synthesized at 0.6 mM seem to feature the right qualities on both counts: particle size and crystal quality. Reaction temperature is also vital behind nucleation and crystallisation. For Fe-MOF-525(SAS), a crystalline MOF is obtained at RT with assistance of SBUs, while the lower temperature suppresses crystal growth rate, culminating in smaller nanoMOF crystals (Figures S20–S22, Supporting Information). This observation is found to be in agreement with literature reports.[31] This reveals a specific advantage of the SAS method as regards forming crystalline nanoMOFs at RT. An adequate reaction time is critical to efficiently sustain a) nucleation; b) crystalline growth. Herein, we successfully construct Fe-MOF-525(SAS) at a reaction time of only 1 h with reduced crystallinity. 3 h is found sufficient to afford the crystalline nanoMOF and a further prolonged reaction time of 12 h negligibly impacts the crystallinity and particle size (Figures S23–S25, Supporting Information). This is likely credited to an accelerated reaction kinetics augmented by the SBUs, thereby completing MOF nucleation and growth in a short time.[22a]

Upon characterising the prepared Fe-MOF-525(SAS), as a proof-of-concept study, we critically examine their electrochemical biosensing properties with regard to the detection of a typical biotoxin, uric acid (UA). For this purpose, a smooth, dense and homogeneous Fe-MOF-525(SAS) film is integrated onto conductive ITO surfaces as Fe-MOF-525(SAS)/ITO electrode (Figures S26–S27, Supporting Information). Herein, a cyclic voltammetry (CV) based sensing is achieved based on the corresponding electrical current. The latter originates from analyte-specific redox reactions under the applied electrochemical potentials.[5b,32] Chasing after CV based sensing, the critical parameters, e.g., scan rate, pH, accumulation time, and loading amounts are optimized. It also offers us to study Fe-MOF-525 particle size effects on its sensing performance. Furthermore, selectivity, practicality, stability, recyclability and reproducibility are investigated comprehensively.

As the final product of purine metabolism, UA plays an important role in biological processes and possesses significant influences on human health. Its prolonged bioaccumulation may cause diseases such as gout and hyperuricemia.[33] Therefore, rapid and efficient detection of UA in biological fluids is a matter of high pathological relevance, especially in clinical diagnosis. Herein, as an electrochemical biosensor for UA detection, the Fe-MOF-525(SAS)/ITO electrode is studied and the corresponding sensitivity and selectivity of detection are evaluated. In the absence of UA, there is no obvious current signal observed on the CV curve (**Figure 2**a). In contrast, the Fe-MOF-525(SAS)/ITO electrode exhibits a sharp, irreversible oxidation peak at 0.67 V in the presence of 100 μM UA. This could be assigned to the electrochemical oxidation of UA to quinonoid diimine, concomitant with the transfer of two protons and electrons (Figure 2b).[33a,34] Predicated upon oxidation, the modified electrode shows prospect as an electrochemical sensor for UA detection. The detailed processes and plausible mechanisms driving electrocatalytic UA oxidation on Fe-MOF-525(SAS)/ITO can be described as follows: 1) thanks to its high surface areas, large micropores of Fe-MOF-525(SAS) facilitates the aggregation of UA molecules; 2) the porphyrin subunits are intrinsically redox-active, conducive to electrochemically sense the redox-active UA analytes. Under an external voltage, the porphyrin centers of Fe-MOF-525(SAS) serve as electron acceptors. Meanwhile, thanks to the electron-donating imino groups, UA can act as an electron donor, interacting with the porphyrin centres to afford an electron donor-acceptor (EDA) system between the porphyrin centres and the UA molecules. This EDA is further evidenced by the UV–vis spectra (Figure S28, Supporting Information).[35] Furthermore, in Fe-MOF-525(SAS), the Zr_6-oxo cluster derived SBUs are known to be insulating in nature. Such redox inactivity nullifies the possibility of charge transfer between Fe-TCPP and the SBUs, as revealed in the UV–vis spectra (Figure S29, Supporting Information).[36] To this end, periodically arranged redox Fe-TCPP centers with a short spatial distance (13.6 Å) afford an efficient redox-hopping in Fe-MOF-525(SAS).[36] The EDA system triggers sequential electron transfer along a redox-hopping approach, followed by deprotonation, thus culminating in the oxidation of UA (Figure 2b and Figure S30, Supporting Information).[5b,20,33a,36]
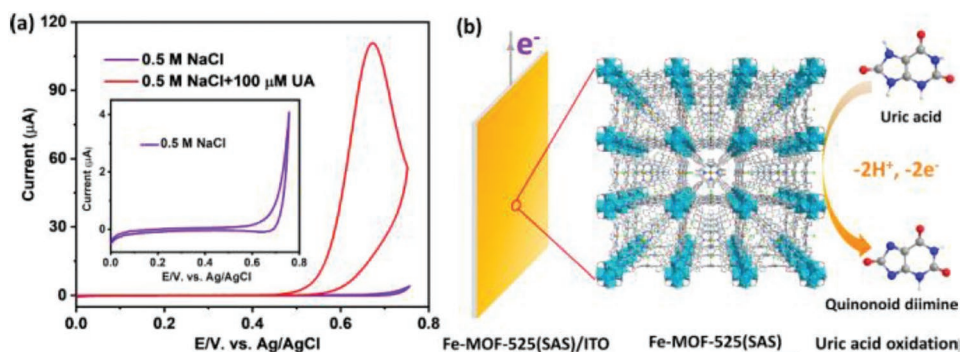
Figure 2. a) CV profiles of the Fe-MOF-525(SAS)/ITO electrode in 0.5 M NaCl solution in the presence or absence of 100 µM UA at a scan rate of 50 mV s^{-1}. Inset: an enlarged CV curve obtained in the absence of 100 µM UA for clear comparison. b) Schematic illustration of the plausible mechanism of UA oxidation on the Fe-MOF-525(SAS)/ITO electrode.

To assess the UA sensing parameters of Fe-MOF-525(SAS)/ITO electrode, performance on bare ITO is explored in tandem (Figure S31, Supporting Information). A weak current response indicates its poor electrocatalytic activity toward UA and in turn, highlights the excellent electrochemical behaviour of Fe-MOF-525(SAS) in the modified electrode. Other metallated M-MOF-525(SAS) (M = Cu, Co, Ni, and Mn) and non-metallated H$_2$-MOF-525(SAS) variants modified electrodes are also prepared separately for comparative analysis (Figures S32 and S33, Supporting Information). Among the variants, Fe-MOF-525(SAS)/ITO delivers the best performance with a higher current response at lower oxidation potential and therefore, ranks as the front runner for UA oxidation. Meanwhile, Fe-MOF-525(SAS) nanoparticles formed at different experimental conditions are parallelly integrated as electrodes for comparison (Table S1, Figures S34–S37, Supporting Information). Of particular importance is Fe-MOF-525(SAS) synthesized following the typical recipe (Exp.1 in Table S1, Supporting Information), that exhibits UA oxidation likely due to its optimised advantages on both the crystal quality and small particle size (Figures S13–S25, Supporting Information). A combination of these can unify high external surfaces with more accessible catalytic sites.

The impact of scan rate on the oxidation current and potential of UA is determined by cyclic voltammetry (Figure S38, Supporting Information). The peak current exhibits a highly linear relationship with the square root of scan rate, characteristic of a diffusion-controlled UA oxidation at the modified electrode.[33c] Meanwhile, the electron transfer number for anodic UA oxidation is estimated as 1.99 according to Laviron's equation,[37] suggesting a 2 electrons transfer process. On the other hand, the chronoamperometric responses of Fe-MOF-525(SAS)/ITO toward different UA concentrations reveal the diffusion coefficient for UA to be 1.850×10^{-4} cm^2 s^{-1} based on Cottrell's equation (Figure S39, Supporting Information).[5b,11c] Another crucial parameter, i.e., electrolyte pH, is also optimized herein (Figure S40, Supporting Information). The maximum peak-current response is achieved at pH 6.5. Hence, pH 6.5 is chosen as the optimum pH for further UA detection. Moreover, with increasing pH, the oxidation peak potential (E_p) shows a linear shift to negative value, following the equation $E_p(V) = -0.0586$ pH $+ 1.032$. The slope of 58.6 mV pH^{-1} is found to be in close agreement with the theoretical Nernstian value, 59 mV pH^{-1}, suggesting an equal number of protons and electrons transferred during UA oxidation.[5b,38] The influence of catalyst loading amount is evaluated by altering the volume (5–50 µL) of MOF suspension (3 mg mL^{-1}) coated on ITO. SEM images reveal the formation of dense and smooth films on electrodes, with increased thickness (Figures S41 and S42, Supporting Information). With the increase of loading amount, the peak current increases and maintains nearly steady values after 30 µL loading (Figure S43, Supporting Information). Therefore, loading of 30 µL Fe-MOF-525(SAS) suspension surfaces a right choice to efficiently detect UA. Accumulation time, as a factor of influence, is studied by adjusting the accumulation times just before measuring the cyclic voltammograms. As shown in the Figure S44 (Supporting Information), nearly constant current peak values are observed after an accumulation time of 120 s, attributed to plausible UA saturation on the modified electrode under a dynamic equilibrium. This is why 120 s is regarded as the optimum accumulation time in our further studies.

The feasibility of Fe-MOF-525(SAS)/ITO electrode for UA detection is examined under optimized conditions with varying concentrations of UA (**Figure 3**a; zoomed views of the low concentrations in Figure S45, Supporting Information). The corresponding oxidation peak currents (I) increased linearly with the increase in UA concentration (c) ranging from 0.05 up to 100 µM with high correlation coefficients ($R^2 > 0.999$). Meanwhile, the sensitivity is estimated to be 1.0956 µA µM^{-1} and the limit of detection (LOD) is determined as low as 0.013 µM ($3 \times S_b$/slope, Figure S46, Table S2, Supporting Information). Compared to the hitherto reported electrodes for UA detection, the proposed Fe-MOF-525(SAS)/ITO electrode sets a benchmark analytical response toward UA in terms of a wide linear response, high sensitivity and low LOD (Table S3, Supporting Information). Its superb electrocatalytic activity toward UA detection stands out, and could be correlated to its high surface area, expedited preconcentration, and the small particle size concomitant with high density of accessible active sites in Fe-MOF-525(SAS) nanoMOF.[5b,12b,13b]

As confirmed in previous reports, the electrocatalytic activity of MOF shows strong dependence on the particle sizes, while the origin of size effects is still in vague declaration.[12,13b] To reasonably investigate the particle size effects of Fe-MOF-525 on UA detection and concurrently reveal the superiority of SAS strategy on advanced sensor preparation, another two Fe-MOF-525 particles herein are synthesized by the CSS method and
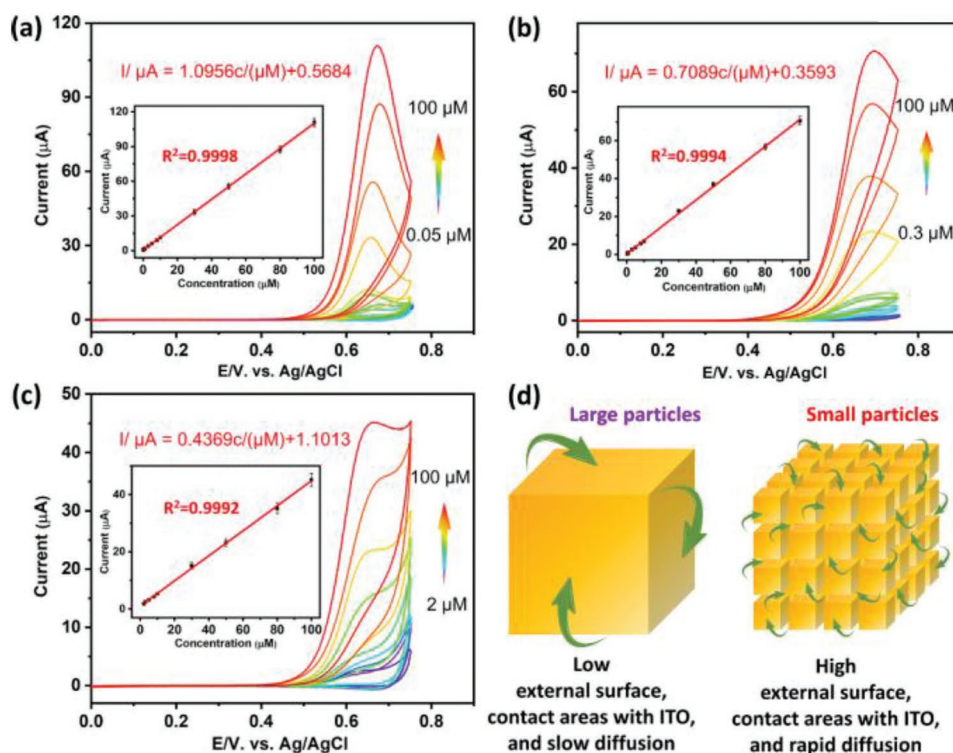
Figure 3. CV curves of the a) Fe-MOF-525(SAS)/ITO, b) Fe-MOF-525(CSS1)/ITO, and c) Fe-MOF-525(CSS2)/ITO electrodes toward the detection of UA at different concentrations; inset shows the linear trend of the peak current versus concentration of corresponding analytes. d) Schematic illustration of the MOFs particle size effects on the UA sensing.

integrated on ITO as Fe-MOF-525(CSS1)/ITO and Fe-MOF-525(CSS2)/ITO electrodes for comparative UA sensing. These two electrodes are modified with equal amount of Fe-MOF-525 crystals as the Fe-MOF-525(SAS)/ITO and their corresponding UA detection performances are also examined under same conditions. Compared to the dense and smooth film of Fe-MOF-525(SAS) nanoparticles (≈30 nm), Fe-MOF-525(CSS1) and Fe-MOF-525(CSS) feature much large sizes of ≈145 and ≈764 nm, respectively, and thus result in awfully rough film state with numbers of cracks and even with a low surface coverage (Figures S27 and S47, Supporting Information). These worse film quality would largely decrease the effective contact area with the underlying ITO substrate, and therefore anticipated to hamper the efficient charge transfer for splendid UA oxidation.[12b] As expected, the Fe-MOF-525(CSS1)/ITO affords a linear response to UA (0.3–100 μM) with the inferior sensitivity of 0.7089 μA μM^{-1} and LOD as 0.092 μM (Figure 3b and Figures S48 and S49, Table S4, Supporting Information). Notably, the Fe-MOF-525(CSS2)/ITO with the largest size shows a further decreased sensitivity (0.4369 μA μM^{-1}) on the UA detection (0.08–100 μM) with a worse LOD of 0.723 μM (Figure 3c and Figures S50 and S51, Table S5, Supporting Information). Following the comparison of UA electrochemical sensing, a distinct size effect stands out. Apart from the contact area, another key point, i.e., enhanced external surface, contributes to the superiority of nanocrystallites on electrocatalytic efficiency. Downsizing the particles can directly increase their external surface areas, thus allowing the exposure of more external active sites (Figure 3d).[13b] This is surely favorable to

the electrocatalytic UA sensing. In addition, high external surface areas of nanocrystals also offer more shortcuts around the increased cubic facets and, therefore, enable a more rapid and efficient diffusion for ample UA molecules to access the internal active sites in channels (Figure 3d).[12b,31c,39] To further confirm the hypothesis, chronoamperometric studies are performed to evaluate the diffusion coefficients of UA in the MOFs with different particle sizes (Figure S52, Supporting Information). According to the Cottrell's equation, the diffusion coefficients for UA are estimated to be 1.8505×10^{-4} cm^2 s^{-1}, 5.692×10^{-5} cm^2 s^{-1}, and 1.0537×10^{-5} cm^2 s^{-1} for Fe-MOF-525(SAS), Fe-MOF-525(CSS1) and Fe-MOF-525(CSS2), respectively. These results clearly verify the rapid UA diffusion owe to the small crystal size. Simply put, particle size effects herein originate from the high external surface, contact area with ITO and rapid analyte diffusion, which contribute to the combination of abundant analyte molecules, more accessible catalytic sites and efficient charge transfer, thus synergistically affording the superior sensing performance.

The positive size effects are evidenced in nanoMOF particles and endow Fe-MOF-525(SAS)/ITO with the upside potential as an efficient electrochemical biosensor. To further evaluate its feasibility, we examined the selectivity of the modified electrode toward UA in the presence of some other typical interferents (Figure S53, Supporting Information). It is observed that common inorganic ions only cause negligible effects (<2%) and biological compounds induce scanty interference (<5%) on the UA sensing performance. Proved by these results, the potential of Fe-MOF-525(SAS)/ITO for selective UA detection becomes

clear, even in the presence of excess these potentially interfering species.

In order to assess the practical viability, the modified electrode is applied to detect UA in the human urine sample. The urine sample was diluted 100 folds with 0.5 M NaCl solution before the measurement and with three sequential addition of 10 μM UA for analysis (Table S6, Supporting Information). The Fe-MOF-525(SAS)/ITO electrode exhibits appropriate recoveries toward UA detection (97.3–99.5%) in real samples, indicating its applicability and reliability as UA biosensor.[33a,b]

As electrochemical sensors, several crucial aspects, viz. material stability, recyclability and reproducibility are also inspected. The excellent stability of Fe-MOF-525(SAS)/ITO is affirmed by the retention of nearly 96.16% of its original response after 60 days (**Figure 4**a). Remarkably, the electrode also shows the benchmark long-term recyclability with a relative standard deviation (RSD) of only 5.43% on current responses and 90.80% initial response retention for 500 measurement cycles (Figure 4c). The high stability evidently stems from the stable Zr_6 clusters and strong chelating effect between Fe(III) and the porphyrin rings.[5b,14a] In addition, comprehensive comparisons on the XRD patterns, SEM images, and UV–vis spectra of the modified electrodes unveils identical crystallinity. Despite identical coating conditions, same molecular structures before and after consecutive detection cycles indeed suggest its outstanding electrochemical and mechanical stability (Figure 4b and

Figure S54–S55). Moreover, ten independent Fe-MOF-525(SAS)/ITO electrodes are examined. A RSD as low as 2.35% (Table S7, Supporting Information) is achieved, indicating superb reproducibility of the modified electrode.

3. Conclusion

In summary, SBU-assisted synthesis is harnessed to quickly prepare nanoparticles of high-connected Fe-MOF-525 at room temperature. The preformed SBUs not only reduce activation energy barrier for framework assembly at RT, but also function as nuclei leading to rapid nucleation and growth terminating in the formation of small nanoMOF crystals. The obtained Fe-MOF-525(SAS) features a particle size of ≈30 nm, much smaller than the ones formed by CSS. After integrated as smooth and dense film on the ITO glass, Fe-MOF-525(SAS)/ITO electrode affords as an electrochemical biosensor. The modified electrode shows record-high voltammetric sensing of UA. Besides the intrinsically periodic and porous architecture with ordered metalloporphyrin active sites, the Fe-MOF-525(SAS) nanoMOF also manifests distinct particle size effects characterized by the high external surface, contact area with ITO and rapid analyte diffusion. All these features together contribute to its benchmark performance in sensitive UA detection with a wide linear range and low LODs. An optimal combination of selectivity,
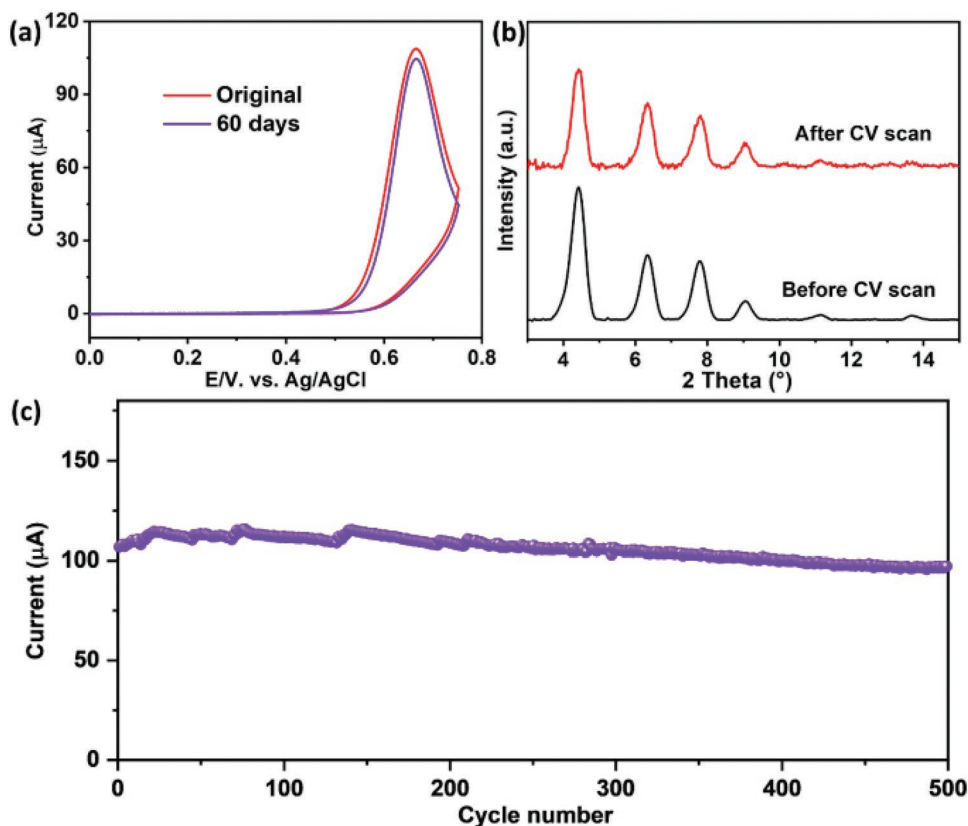

Figure 4. a) CV curves of UA (100 μM) detection on Fe-MOF-525(SAS)/ITO at the initial time and after 60 days. b) GIXRD patterns of the Fe-MOF-525(SAS)/ITO electrodes before and after 10 repetitive cyclic voltammetric scans. c) Recyclability study of a single Fe-MOF-525(SAS)/ITO modified electrode for 500 times long-term recycling detection of UA (100 μM).

ADVANCED
SCIENCE NEWS
www.advancedsciencenews.com

NANO · MICRO
small
www.small-journal.com

stability, long-term recyclability, reproducibility and practicality is validated on the Fe-MOF-525(SAS)/ITO and, therefore, it holds great promise to design efficient electrochemical biosensors in the future. Given such successful example as Fe-MOF-525(SAS), it could be envisioned that the efficient SAS strategy would greatly facilitate the rapid synthesis of small nano-MOFs at RT, and especially exploit their unique size effect in advancing bespoke sensors.

Supporting Information

Supporting Information is available from the Wiley Online Library or from the author.

Conflict of Interest

The authors declare no conflict of interest.

Data Availability Statement

The data that support the findings of this study are available from the corresponding author upon reasonable request.

[1] a) H. Furukawa, K. E. Cordova, M. O'Keeffe, O. M. Yaghi, *Science* **2013**, *341*, 1230444; b) S. R. Batten, N. R. Champness, X.-M. Chen, J. Garcia-Martinez, S. Kitagawa, L. Öhrström, M. O'Keeffe, M. Paik Suh, J. Reedijk, *Pure Appl. Chem.* **2013**, *85*, 1715; c) L. Öhrström, F. M. A. Noa, *Metal-Organic Frameworks*, American Chemical Society, **2021**, https://doi.org/10.1021/acs.infocus.7e4004.

[2] a) D. J. Tranchemontagne, J. L. Mendoza-Cortes, M. O'Keeffe, O. M. Yaghi, *Chem. Soc. Rev.* **2009**, *38*, 1257; b) M. J. Kalmutzki, N. Hanikel, O. M. Yaghi, *Sci. Adv.* **2018**, *4*, 9180.

[3] G. R. Desiraju, *Angew. Chem., Int. Ed.* **1995**, *34*, 2311.

[4] a) M. D. Allendorf, V. Stavila, *CrystEngComm* **2015**, *17*, 229; b) B. Moulton, M. J. Zaworotko, *Chem. Rev.* **2001**, *101*, 1629.

[5] a) C. S. Liu, J. Li, H. Pang, *Coord. Chem. Rev.* **2020**, *410*, 213222; b) Z. Zhou, S. Mukherjee, S. Hou, W. Li, M. Elsner, R. A. Fischer, *Angew. Chem., Int. Ed.* **2021**, *60*, 20551.

[6] a) Q. Wang, D. Astruc, *Chem. Rev.* **2020**, *120*, 1438; b) Y.-B. Huang, J. Liang, X.-S. Wang, R. Cao, *Chem. Soc. Rev.* **2017**, *46*, 126; c) A. L. Semrau, Z. Zhou, S. Mukherjee, M. Tu, W. Li, R. A. Fischer, *Langmuir* **2021**, *37*, 6847.

[7] a) B. M. Connolly, M. Aragones-Anglada, J. Gandara-Loe, N. A. Danaf, D. C. Lamb, J. P. Mehta, D. Vulpe, S. Wuttke, J. Silvestre-Albero, P. Z. Moghadam, *Nat. Commun.* **2019**, *10*, 2345; b) Z. Zhou, B. Cheng, C. Ma, F. Xu, J. Xiao, Q. Xia, Z. Li, *RSC Adv.* **2015**, *5*, 94276.

[8] a) J. Wang, Y. Zhang, P. Zhang, J. Hu, R. B. Lin, Q. Deng, Z. Zeng, H. Xing, S. Deng, B. Chen, *J. Am. Chem. Soc.* **2020**, *142*, 9744; b) Z. Zhou, L. Mei, C. Ma, F. Xu, J. Xiao, Q. Xia, Z. Li, *Chem. Eng. Sci.* **2016**, *147*, 109.

[9] J. Chen, Y. Zhu, S. Kaskel, *Angew. Chem., Int. Ed.* **2021**, *60*, 5010.

[10] H. Lee, K.-I. Hong, W.-D. Jang, *Coord. Chem. Rev.* **2018**, *354*, 46.

[11] a) Y. Wang, M. Zhao, J. Ping, B. Chen, X. Cao, Y. Huang, C. Tan, Q. Ma, S. Wu, Y. Yu, Q. Lu, J. Chen, W. Zhao, Y. Ying, H. Zhang, *Adv. Mater.* **2016**, *28*, 4149; b) Y. Chen, X. Sun, S. Biswas, Y. Xie, Y. Wang, X. Hu, *Biosens. Bioelectron.* **2019**, *141*, 111470; c) S. Biswas, Y. Chen, Y. Xie, X. Sun, Y. Wang, *Anal. Chem.* **2020**, *92*, 4566.

[12] a) Y. Zhao, L. Jiang, L. Shangguan, L. Mi, A. Liu, S. Liu, *J. Mater. Chem. A* **2018**, *6*, 2828; b) C. H. Su, C. W. Kung, T. H. Chang, H. C. Lu, K. C. Ho, Y. C. Liao, *J. Mater. Chem. A* **2016**, *4*, 11094.

[13] a) S. Wang, C. M. McGuirk, A. d'Aquino, J. A. Mason, C. A. Mirkin, *Adv. Mater.* **2018**, *30*, 1800202; b) M. Chang, Y. Wei, D. Liu, J. X. Wang, J. F. Chen, *Angew. Chem., Int. Ed.* **2021**, *60*, 26390.

[14] a) W. Morris, B. Volosskiy, S. Demir, F. Gandara, P. L. McGrier, H. Furukawa, D. Cascio, J. F. Stoddart, O. M. Yaghi, *Inorg. Chem.* **2012**, *51*, 6443; b) S. Rojas-Buzo, B. Bohigues, C. W. Lopes, D. M. Meira, M. Boronat, M. Moliner, A. Corma, *Chem. Sci.* **2021**, *12*, 10106; c) G. F. Hassan, N. El Hoda Saad, M. Hmadeh, P. Karam, *Dalton Trans.* **2018**, *47*, 15765.

[15] Z. Chen, M. C. Wasson, R. J. Drout, L. Robison, K. B. Idrees, J. G. Knapp, F. A. Son, X. Zhang, W. Hierse, C. Kühn, S. Marx, B. Hernandez, O. K. Farha, *Faraday Discuss.* **2021**, *225*, 9.

[16] a) S. Geng, E. Lin, X. Li, W. Liu, T. Wang, Z. Wang, D. Sensharma, S. Darwish, Y. H. Andaloussi, T. Pham, P. Cheng, M. J. Zaworotko, Y. Chen, Z. Zhang, *J. Am. Chem. Soc.* **2021**, *143*, 8654; b) S. Dai, F. Nouar, S. Zhang, A. Tissot, C. Serre, *Angew. Chem., Int. Ed.* **2021**, *60*, 4282; c) P. Zhang, X. Kang, L. Tao, L. Zheng, J. Xiang, R. Duan, J. Li, P. Chen, X. Xing, G. Mo, Z. Wu, B. Han, *CCS Chem.* **2022**, https://doi.org/10.31635/ccschem.022.202202155.

[17] a) T. Kundu, S. Mitra, P. Patra, A. Goswami, D. Díaz Díaz, R. Banerjee, *Chem. - Eur. J.* **2014**, *20*, 10514; b) N. A. Khan, I. J. Kang, H. Y. Seok, S. H. Jhung, *Chem. Eng. J.* **2011**, *166*, 1152; c) P. D. Morris, I. J. McPherson, M. A. Edwards, R. J. Kashtiban, R. I. Walton, P. R. Unwin, *Angew. Chem., Int. Ed.* **2020**, *59*, 19696; d) X. G. Wang, Q. Cheng, Y. Yu, X. Z. Zhang, *Angew. Chem., Int. Ed.* **2018**, *57*, 7836; e) M. Zhao, Y. Wang, Q. Ma, Y. Huang, X. Zhang, J. Ping, Z. Zhang, Q. Lu, Y. Yu, H. Xu, Y. Zhao, H. Zhang, *Adv. Mater.* **2015**, *27*, 7372; f) T. Tsuruoka, S. Furukawa, Y. Takashima, K. Yoshida, S. Isoda, S. Kitagawa, *Angew. Chem., Int. Ed.* **2009**, *48*, 4739.

[18] a) J. L. Zhuang, D. Ceglarek, S. Pethuraj, A. Terfort, *Adv. Funct. Mater.* **2011**, *21*, 1442; b) G. Majano, J. Perez-Ramirez, *Adv. Mater.* **2013**, *25*, 1052; c) H. Zhao, H. Song, L. Chou, *Mater. Chem. Phys.* **2014**, *143*, 1005; d) M. Zhu, S. R. Venna, J. B. Jasinski, M. A. Carreon, *Chem. Mater.* **2011**, *23*, 3590.

[19] a) S. M. Yoon, J. H. Park, B. A. Grzybowski, *Angew. Chem., Int. Ed.* **2017**, *129*, 133; b) D. Feng, Z. Y. Gu, J. R. Li, H. L. Jiang, Z. Wei, H. C. Zhou, *Angew. Chem., Int. Ed.* **2012**, *51*, 10307; c) D. Feng, Z. Y. Gu, Y. P. Chen, J. Park, Z. Wei, Y. Sun, M. Bosch, S. Yuan,

ADVANCED
SCIENCE NEWS

www.advancedsciencenews.com

NANO · MICRO

small

www.small-journal.com

H. C. Zhou, *J. Am. Chem. Soc.* **2014**, *136*, 17714; d) Z. Zhou, S. Mukherjee, J. Warnan, W. Li, S. Wannapaiboon, S. Hou, K. Rodewald, B. Rieger, P. G. Weidler, C. Wöll, R. A. Fischer, *J. Mater. Chem. A* **2020**, *8*, 25941.

[20] I. Hod, M. D. Sampson, P. Deria, C. P. Kubiak, O. K. Farha, J. T. Hupp, *ACS Catal.* **2015**, *5*, 6302.

[21] M. Eddaoudi, D. B. Moler, H. Li, B. Chen, T. M. Reineke, M. O'keeffe, O. M. Yaghi, *Acc. Chem. Res.* **2001**, *34*, 319.

[22] a) O. Shekhah, H. Wang, D. Zacher, R. A. Fischer, C. Woll, *Angew. Chem., Int. Ed.* **2009**, *48*, 5038; b) V. Guillerm, S. Gross, C. Serre, T. Devic, M. Bauer, G. Ferey, *Chem. Commun.* **2010**, *46*, 767.

[23] a) M. R. DeStefano, T. Islamoglu, S. J. Garibay, J. T. Hupp, O. K. Farha, *Chem. Mater.* **2017**, *29*, 1357; b) H. Noh, C.-W. Kung, T. Islamoglu, A. W. Peters, Y. Liao, P. Li, S. J. Garibay, X. Zhang, M. R. DeStefano, J. T. Hupp, O. K. Farha, *Chem. Mater.* **2018**, *30*, 2193; c) H. He, L. Li, Y. Liu, M. Kassymova, D. Li, L. Zhang, H. L. Jiang, *Nano Res.* **2020**, *14*, 444.

[24] a) T. Y. Huang, C. W. Kung, Y. T. Liao, S. Y. Kao, M. Cheng, T. H. Chang, J. Henzie, H. R. Alamri, Z. A. Alothman, Y. Yamauchi, K. C. Ho, K. C. Wu, *Adv. Sci.* **2017**, *4*, 1700261; b) C. W. Kung, Y. S. Li, M. H. Lee, S. Y. Wang, W. H. Chiang, K. C. Ho, *J. Mater. Chem. A* **2016**, *4*, 10673.

[25] G. Kickelbick, U. Schubert, *Chem. Ber.* **1997**, *130*, 473.

[26] K. S. Walton, R. Q. Snurr, *J. Am. Chem. Soc.* **2007**, *129*, 8552.

[27] L. Shi, L. Yang, H. Zhang, K. Chang, G. Zhao, T. Kako, J. Ye, *Appl. Catal. B* **2018**, *224*, 60.

[28] L. Feng, K. Y. Wang, J. Powell, H.-C. Zhou, *Matter* **2019**, *1*, 801.

[29] H. Zhang, J. Wei, J. Dong, G. Liu, L. Shi, P. An, G. Zhao, J. Kong, X. Wang, X. Meng, J. Zhang, J. Ye, *Angew. Chem., Int. Ed.* **2016**, *55*, 14310.

[30] S. Diring, S. Furukawa, Y. Takashima, T. Tsuruoka, S. Kitagawa, *Chem. Mater.* **2010**, *22*, 4531.

[31] a) T. Chalati, P. Horcajada, R. Gref, P. Couvreur, C. Serre, *J. Mater. Chem.* **2011**, *21*, 2220; b) H. Bunzen, M. Grzywa, M. Hambach, S. Spirkl, D. Volkmer, *Cryst. Growth Des.* **2016**, *16*, 3190; c) M. Zhong,

L. Kong, K. Zhao, Y. H. Zhang, N. Li, X. H. Bu, *Adv. Sci.* **2021**, *8*, 2001980.

[32] a) J. F. Rusling, S. L. Suib, *Adv. Mater.* **1994**, *6*, 922; b) N. Elgrishi, K. J. Rountree, B. D. McCarthy, E. S. Rountree, T. T. Eisenhart, J. L. Dempsey, *J. Chem. Educ.* **2017**, *95*, 197.

[33] a) B. Kulyk, S. O. Pereira, A. J. S. Fernandes, E. Fortunato, F. M. Costa, N. F. Santos, *Carbon* **2022**, *197*, 253; b) W. Zhang, L. Liu, Y. Li, D. Wang, H. Ma, H. Ren, Y. Shi, Y. Han, B. C. Ye, *Biosens. Bioelectron.* **2018**, *121*, 96; c) Z. Xu, J. Song, B. Liu, S. Lv, F. Gao, X. Luo, P. Wang, *Sens. Actuators, B* **2021**, *348*, 130674.

[34] a) R. Goyal, A. Brajter-Toth, G. Dryhurst, *J. Electroanal. Chem. Interfacial Electrochem.* **1982**, *131*, 181; b) X. Wei, M. Zhu, J. Li, L. Liu, J. Yu, Z. Li, B. Ding, *Nano Energy* **2021**, *85*, 106031.

[35] a) M. Jahan, Q. Bao, K. P. Loh, *J. Am. Chem. Soc.* **2012**, *134*, 6707; b) S. Iseki, K. Nonomura, S. Kishida, D. Ogata, J. Yuasa, *J. Am. Chem. Soc.* **2020**, *142*, 15842.

[36] a) S. R. Ahrenholtz, C. C. Epley, A. J. Morris, *J. Am. Chem. Soc.* **2014**, *136*, 2464; b) A. Cadiau, L. S. Xie, N. Kolobov, A. Shkurenko, M. Qureshi, M. R. Tchalala, S. S. Park, A. Bavykina, M. Eddaoudi, M. Dincă, C. H. Hendon, J. Gascon, *Chem. Mater.* **2019**, *32*, 97; c) C. W. Kung, S. Goswami, I. Hod, T. C. Wang, J. Duan, O. K. Farha, J. T. Hupp, *Acc. Chem. Res.* **2020**, *53*, 1187; d) P. A. Herrera-Herrera, E. Rodriguez-Sevilla, A. S. Varela, *Dalton Trans.* **2021**, *50*, 16939; e) K. Maindan, X. Li, J. Yu, P. Deria, *J. Phys. Chem. B* **2019**, *123*, 8814; f) L. Sun, M. G. Campbell, M. Dinca, *Angew. Chem., Int. Ed.* **2016**, *55*, 3566; g) J. H. Li, Y. S. Wang, Y. C. Chen, C. W. Kung, *Appl. Sci.* **2019**, *9*, 2427.

[37] E. Laviron, *J. Electroanal. Chem. Interfacial Electrochem.* **1974**, *52*, 355.

[38] R. Ojani, A. Alinezhad, Z. Abedi, *Sens. Actuators, B* **2013**, *188*, 621.

[39] a) O. M. Linder-Patton, T. J. de Prinse, S. Furukawa, S. G. Bell, K. Sumida, C. J. Doonan, C. J. Sumby, *CrystEngComm* **2018**, *20*, 4926; b) O. M. Linder-Patton, W. M. Bloch, C. J. Coghlan, K. Sumida, S. Kitagawa, S. Furukawa, C. J. Doonan, C. J. Sumby, *CrystEngComm* **2016**, *18*, 4172.